



Remote Estimation of Turbulence Intensity Variation in Open Channels

Erika D. Johnson¹ and Edwin A. Cowen, Ph.D., M.ASCE²

Abstract: The open channel flow community has a history of using a set of universal exponential expressions to describe the vertical variation of turbulence intensity in open channel flows. All of these relationships contain an empirical coefficient that varies with the component direction ($D_u = 2.3$, $D_v = 1.27$, $D_w = 1.63$). Recent laboratory experiments have demonstrated that for smooth and rough bed open channel flows, these constants are not universal but vary with the Reynolds number, bed composition, and in the presence of streamwise counter-rotating vortices and secondary flows. A robust method for the remote prediction of D_u , and hence the vertical variation of the streamwise turbulence intensity is developed here for a wide range of flow conditions. The method uses the free-surface turbulence anisotropy as a proxy for the redistribution of vertical velocity fluctuations into surface-parallel components, enabling a correlation between the free-surface turbulence intensity and D_u . Implications for the remote prediction of bed composition, sediment transport, and bed shear stress are discussed. DOI: 10.1061/(ASCE)HY.1943-7900.0001774. © 2020 American Society of Civil Engineers.

Introduction

Following a series of tilting open channel flow experiments, Nezu (1977) established a set of universal exponential expressions to describe the vertical variation of the turbulence intensities in the form

$$\begin{aligned} \frac{u'}{u^*} &= D_u \exp(-z/H), \\ \frac{v'}{u^*} &= D_v \exp(-z/H), \\ \frac{w'}{u^*} &= D_w \exp(-z/H) \end{aligned} \quad (1)$$

where u' , v' , w' = streamwise, lateral, and vertical turbulence root-mean square (RMS) velocities, respectively. (Alternatively, throughout this work the RMS velocity will be referred to as the turbulence fluctuation.) The friction velocity is designated by u^* , H is the flow depth, and z is the vertical direction, positive upward, with the zero-reference level at the bed. Each of these relationships contains an empirical coefficient that varies with the component direction ($D_u = 2.3$, $D_v = 1.27$, $D_w = 1.63$). The authors note here that a difference in coordinate systems between Nezu (1977) and that used in this work (namely, using the z -axis to indicate the vertical component direction rather than the y -axis) results in the difference between our reported values and Nezu's (1977) ($D_v = 1.63$, $D_w = 1.27$). The flow depth for Nezu's (1977) experiments ranged from $H = 0.02$ to 0.08 m, the channel aspect ratio ranged from $B/H = 6$ to 23 (where B is the channel width), and the bulk mean velocity ($U_m = Q/A$, where Q is the

volumetric discharge rate and A is the channel cross-sectional area) for smooth bed cases ranged from $U_m = 0.40$ to 1.4 m/s and $U_m = 0.13$ – 0.15 m/s for the rough bed cases [$R = (U_m H)/\nu = 8,600$ – $46,200$]. The Froude number for Nezu's experiments was 0.46 – 3.12 .

Since these seminal experiments were carried out, a number of researchers have reported their measured values for these constants (Table 1), and variation has been observed. Published values fall in ranges of $D_u = 0.97$ – 3.02 , $D_v = 1.39$ – 1.89 , and $D_w = 1.04$ – 1.67 . Although not every study reports a best-fit coefficient for the vertical variation of the turbulent intensities in the streamwise direction or the other component directions, variation from Nezu's (1977) relations has been observed in data plotted against these relations [e.g., Fig. 11 in Rodríguez and García (2008), Figs. 6 and 7 in Tominaga and Sakaki (2010), Fig. 9(b) in Nikora and Smart (1997), Fig. 12 in Carvalho et al. (2010), Fig. 6 in Cardoso et al. (1989), Figs. 11 and 13 in Nezu and Rodi (1986), and Figs. 7 and 13 in Dittrich and Koll (1997)].

Specifically, discrepancies between Nezu's (1977) universal constants and measured results have been noted in the region close to the bed ($z/H < 0.2$, where z/H is the nondimensional flow depth) (Tominaga and Sakaki 2010) and resulting from secondary flows present in compound open channel flows (Knight and Shiono 1990; see their Figs. 3–5). Rodríguez and García (2008) point out that there is little experimental evidence that these empirical constants are valid under rough bed flow conditions. Indeed, Sukhodolov et al. (1998) state that these constants are not universal and depend on channel bed roughness.

Knowledge of the vertical variation of the turbulent intensities is fundamental to the overall classification of the turbulence environment in open channel flows. It is essential for the remote prediction of bed shear stress in these flows. In Johnson and Cowen (2017) a method was developed to remotely predict bed shear stress by rearranging Nezu's (1977) relation for the vertical distribution of turbulence dissipation to solve for the friction velocity:

$$\begin{aligned} \frac{\langle \varepsilon \rangle H}{u^{*3}} &= \frac{E}{\sqrt{z/H}} \exp(-3z/H) \rightarrow \\ u^* &= \left[\frac{\langle \varepsilon \rangle H}{E} \sqrt{z/H} \exp(3z/H) \right]^{1/3} \end{aligned} \quad (2)$$

¹NRC Research Associate, Naval Research Laboratory, 4555 Overlook Ave., SW, Code 7233, Washington, DC 20375 (corresponding author). ORCID: <https://orcid.org/0000-0002-0685-5558>. Email: erika.johnson.ctr@nrl.navy.mil

²Professor and Director, DeFrees Hydraulics Laboratory, School of Civil and Environmental Engineering, Cornell Univ., 527 College Ave., Ithaca, NY 14853-3501. Email: eac20@cornell.edu

Note. This manuscript was submitted on June 11, 2019; approved on January 24, 2020; published online on July 7, 2020. Discussion period open until December 7, 2020; separate discussions must be submitted for individual papers. This paper is part of the *Journal of Hydraulic Engineering*, © ASCE, ISSN 0733-9429.

Table 1. Reported constants for turbulence intensities

References	Bed condition	Empirical constants		
		D_u	D_v	D_w
Cardoso et al. (1989)	—	2.28	—	—
Carling et al. (2002)	Gravel bed, grass covered gravel, and silt	1.86–2.31	1.41–1.89	1.04–1.62
Dittrich and Koll (1997)	Gravel bed	0.97–3.02	—	—
Johnson and Cowen (2017)	Smooth glass	1.85	1.63	1.27
	Gravel bed	3	—	—
Knight and Shiono (1990)	Smooth cement	2.18	1.39	1.14
Nezu and Rodi (1986)	—	2.26–2.3	—	1.23
Soulsby (1981)	Sand	2.27	1.78	1.21
Sukhodolov et al. (2006)	Mobile bed forms	2.38	1.74	1.38
	Artificial bed form	2.50	1.88	1.40
Sukhodolov et al. (1998)	—	1.96–2.60	1.60–1.88	1.46–1.67
Tominaga et al. (1989)	Painted iron plate	—	1.45	1.15

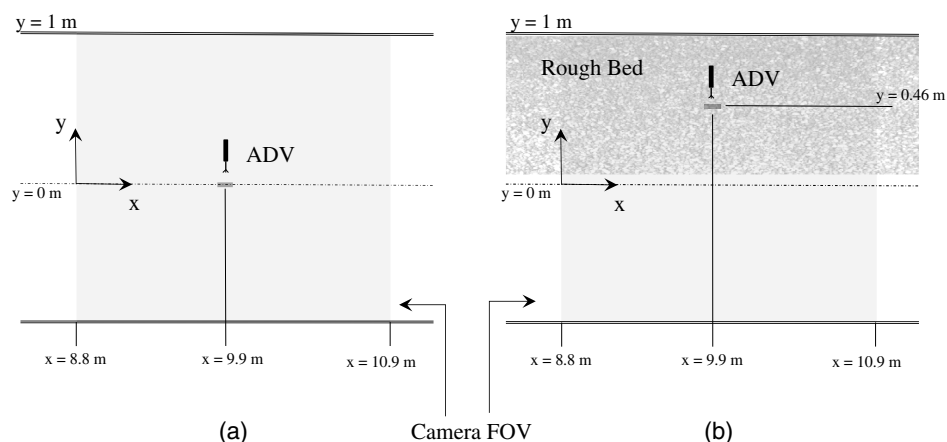
where ε = mean dissipation of turbulent kinetic energy on free surface; $\langle \rangle$ temporal averaging; and E = another of Nezu's empirical constants that is proportional to D_u^3 and was reported to be equal to 9.8 [see Nezu (1977) for the derivation of E and its relation to D_u]. In the Johnson and Cowen (2017) experiments, the best-fit value of D_u was used to determine E , and because the best-fit value of D_u ($D_u = 1.85$, smooth bed, and $D_u = 3$, rough bed) varied from Nezu's established constant, so did the best-fit value of E ($E = 4.76$, smooth bed, $E = 12$, rough bed).

Presently, to use the method of Johnson and Cowen (2017) to remotely predict bed shear stress, in situ measurements of the vertical variation of the streamwise turbulence intensity, u'/u^* , must be made to characterize E . The aim of this paper is to address this need by developing a remote method to characterize the vertical variation of the streamwise turbulence intensities. Remote prediction of the vertical variation of the turbulent intensities is complicated by the fact that near the free surface the vertical turbulent velocity fluctuations, which originate as bursts or ejections from the bed, are redistributed into surface-parallel components (i.e., enhanced u' and v' fluctuations) due to the kinematic constraint the free surface presents. This means that the turbulence intensity that is measured on the free surface may not necessarily be the same as what is measured in the water column. This phenomenon is documented by Cowen et al. (1995) and discussed in this manuscript.

Wide-Open Channel Flume

A series of experiments was conducted in a flat-bottomed, recirculating, wide-open channel flume, described and shown in detail in Johnson (2015) and Johnson and Cowen (2016). The test section of the channel is 15 m long, 2 m wide, and 0.64 m deep. Depicted in Fig. 1 is a top view of the experimental setup. The measurements conducted as part of this investigation were made approximately 9 m downstream from the inlet of the test section to allow sufficient distance for the boundary layer to develop fully. As illustrated in Fig. 1 of Johnson and Cowen (2016), the origin of the coordinate system is located at the beginning of the test section, along the channel centerline, at the channel bed.

Sixteen experimental cases were run in which smooth glass walls formed the bed. For these experiments, the uniform flow depth was varied from 0.06 to 0.31 m (as measured by a Banner S18UUAQ ultrasonic water elevation gauge, Banner Engineering, Plymouth, Minnesota) and the depth-averaged velocity [$U_B = \int_0^H \langle U(z) \rangle / H dz$, where $\langle U(z) \rangle$ is the mean streamwise velocity] was varied from 0.05 to 0.35 m/s, yielding a Reynolds number range of $R_H = (U_B H) / \nu = 5,000$ –74,000 [see Table 1 in Johnson and Cowen (2016)]. Seven experimental cases were conducted with a bed of loose gravel (median diameter: $D_{50} = 56.1$ mm) added to half the channel. Here again, the flow depth was varied from $H = 0.08$ to 0.21 m (the reference level is the glass bed), and a Reynolds number range of $R_H = 5,000$ –52,000 was achieved [see Table 3 and Fig. 4

**Fig. 1.** Top view of experimental setup for (a) smooth bed; and (b) rough bed cases.

in Johnson and Cowen (2016)]. The Froude number for all of these experimental cases is subcritical and ranged from 0.05 to 0.46.

Large-Scale Particle Image Velocimetry Measurements

To quantify the free-surface turbulence intensity, large-scale particle image velocimetry (LSPIV) measurements were conducted for all of the experimental cases. Particle image velocimetry (PIV) is an image-based fluid velocity measurement technique that involves capturing images in rapid succession of, in this case, the free surface of an open channel flow that has been artificially seeded with small buoyant particles. The average displacement of a small cloud of tracer particles is the same as the average displacement of the small region of surface fluid in which they reside. A cross-correlation algorithm (Cowen and Monismith 1997) is used to determine this displacement in pixels. Calibration of the camera allows the pixel displacement to be converted to a physical displacement and, when divided by the elapsed time between successive images, yields an instantaneous surface velocity vector. The instantaneous velocity fields captured in successive images can be averaged in time to determine the mean velocity field. Subtracting the mean field from each instantaneous velocity field produces the instantaneous turbulent velocity fluctuation field.

In these experiments, a 12-bit/pixel IMPERX IGV-B02020 charge-coupled device camera (Imperx, Boca Raton, Florida) with a $2,060 \times 2,056$ pixel array was suspended from the laboratory ceiling (approximately 3 m above the channel bed) and aimed at the free surface. The spatial resolution ranged from 1.01 to 1.08 mm/pixel depending on the flow depth and was determined via camera calibration. The elapsed time between image pairs was $\Delta t = 75\text{--}400$ ms (depending on the flow speed), and approximately 4,000 image pairs were captured at 1 Hz for each experimental condition. Pliolite VTAC-L particles, with a particle diameter of 0.42–0.60 mm, were used as the free-surface tracer material. The analysis of these images was conducted using the cross-correlation algorithm of Cowen and Monismith (1997) with 64×32 pixel subwindows (0.06×0.03 m with the longer direction of the subwindows aligned with the mean flow direction). Further details on the experimental setup for the LSPIV experiments and the cross-correlation algorithm can be found in Johnson (2015) and Johnson and Cowen (2016).

Error analysis was performed on the surface velocities measured by the LSPIV system, and system, and the 95th percentile random error assessed via the bootstrap method was found to be ± 3.1 mm/s (Efron and Tibshirani 1994). The worst-case bias error, which was attributed to calibration errors, was found to be 7 mm/s.

Acoustic Doppler Velocimeter Measurements

In situ measurements characterizing the properties of the flow in the water column were made using a Nortek Vectrino acoustic Doppler velocimeter (ADV) equipped with + firmware. To enable measurements close to the free surface, the ADV was positioned with its axis pointed laterally, i.e., toward the channel side walls. It was then traversed vertically (i.e., normal to the free surface) at 6-mm increments through the water column. For measurements close to the bed and free surface, the vertical increment was decreased to either 3 or 1.5 mm. Due to the lateral positioning of the ADV, it was not able to measure closer than 0.03 m to the bed. The logarithmic law was used to fit and extrapolate the velocity profiles to the bed. For the smooth bed cases, measurements were taken at the channel centerline, $y/B = 0$. The measurements reported here for the rough

bed cases were taken in the center of the gravel bed strip, $y/B = 0.23$ (Fig. 1).

For each experimental condition, the cylindrical measurement volume of the ADV was 6 mm in diameter and 8 mm in length. Five minutes of data were taken at each vertical position at a sample rate of 200 Hz. During postprocessing, the data were passed through a threshold filter and an adaptive Gaussian filter (Cowen and Monismith 1997). The signal-to-noise ratio of these measurements was on average 16 dB, and the correlation values were high ($>93\%$).

Sources of bias error in the ADV measurements include positioning and calibration errors. The worst-case bias error was found to be 0.3 mm/s. The 95th percentile random error assessed via the bootstrap method was found to be ± 0.3 mm/s (Efron and Tibshirani 1994).

Streamwise Coherent Structures and Secondary Flows

With the objective of developing a technique to remotely estimate the vertical variation of the streamwise turbulence intensity, the first step is to develop an understanding of how streamwise counter-rotating vortices and secondary flows influence open channel flow. Streamwise counter-rotating vortices are naturally occurring coherent structures that form in open channels due to the anisotropy of the v' and w' turbulent RMS velocities, which results from the channel geometry. Fig. 5.3 in Nezu and Nakagawa (1993) outlines the complete mechanisms by which these structures are generated. Long time averages of the streamwise counter-rotating structures reveal the secondary flows they generate (Tamburrino and Gulliver 1999).

The size of these structures, as depicted in Fig. 9 of Shvidchenko and Pender (2001), scales with the flow depth. While there seems to be a general consensus on their height and width (also equivalent to the flow depth), a range of values regarding their length has been published in the literature [approximately 1–6 H ; see Table 1 in Roy et al. (2004)]. Shvidchenko and Pender (2001) suggest that, on average, they are approximately (4–5) H long. Shvidchenko and Pender (2001) further found that for their laboratory experiments full development of these depth-scale structures was achieved at a distance equivalent to approximately 25–50 flow depths. Given the range of flow depths for the experimental cases reported herein, 0.06–0.31 m, and the location at which the measurements were taken (approximately 9 m downstream from the beginning of the test section), this means that in the deepest flow case (0.31 m), the secondary flows were likely only marginally developed.

As illustrated in Fig. 9 of Shvidchenko and Pender (2001), streamwise counter-rotating vortex structures rotate about their streamwise and transverse axes. The rotation about the streamwise axis results in an alternating pattern of upwelling and downwelling that occurs with a spatial wavelength equivalent to twice the flow depth. The pattern of upwelling and downwelling results in an undulating pattern in the bed shear stress and in the composition of sandy beds, with finer sand preferentially deposited under regions of upwelling and coarser sand found under downwelling regions [see Fig. 5.19 in Nezu and Nakagawa (1993)]. On the free surface, regions of upwelling are indicated by bands of boils. These are regions of strong divergence, and because near-bed fluid is being brought to the surface in the upwelling regions, these bands are also characterized by lower streamwise mean velocity and high streamwise turbulence intensities. The rotation about the streamwise axis notably influences the vertical variation of the turbulence

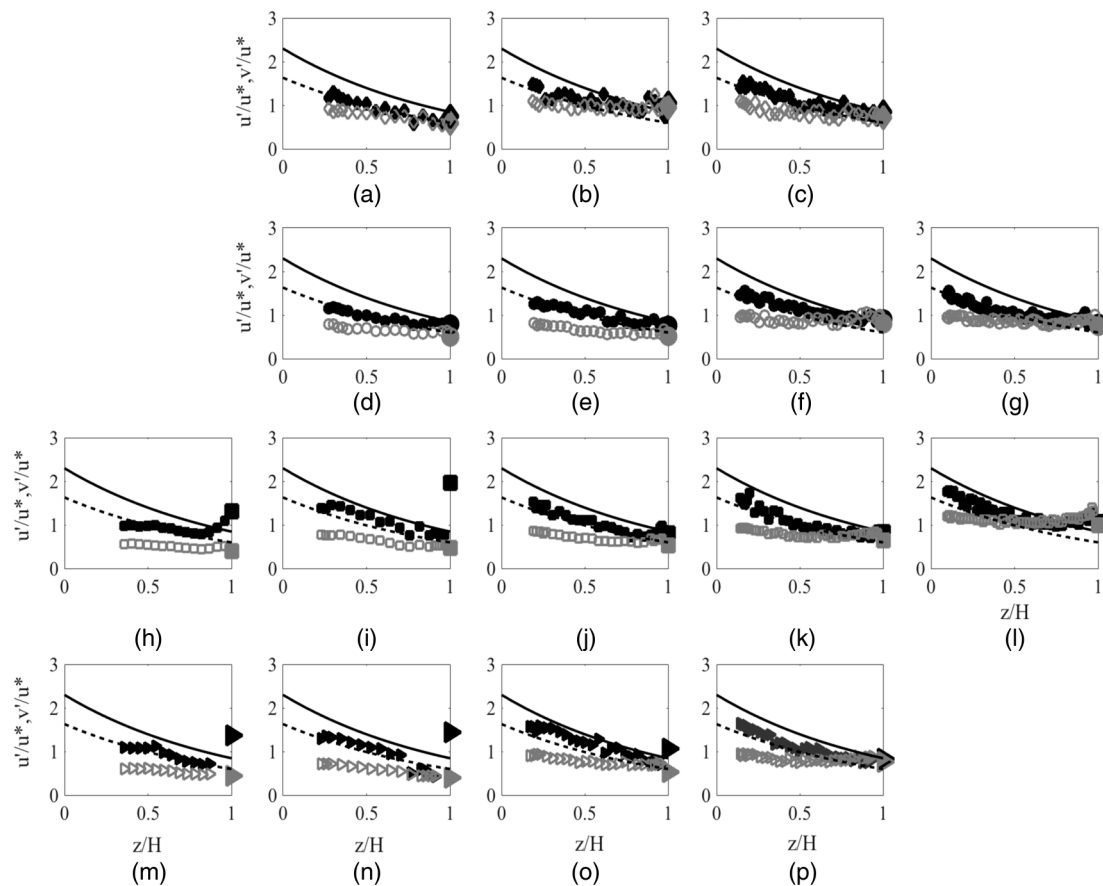


Fig. 2. Turbulent intensities for smooth bed cases, u'/u^* (black symbols) and v'/u^* (gray symbols). Large black (u'/u^*) and gray (v'/u^*) symbols at $z/H = 1$ are surface large-scale particle image velocimetry measurements. Solid black line, $u'/u^* = 2.3 \exp(-z/H)$; dashed black line, $v'/u^* = 1.63 \exp(-z/H)$. (Equation from Nezu 1977.)

intensity by increasing its magnitude above Nezu's exponential relation in the region of the free surface. This effect can be seen in Fig. 2 and will be discussed further in the next section. Table 5.2 in Nezu and Nakagawa (1993) provides an excellent summary of the effects that secondary flow structures have on the overall flow.

Tamburrino and Gulliver (1999) predicted that for a given channel aspect ratio, B/H , the number of upwelling and downwelling regions will be given by the following expressions:

$$\begin{aligned} \text{Downwelling regions: even integer in range } & \frac{(B/H)}{2} \text{ to } \frac{(B/H)}{3} \\ \text{Upwelling regions: odd integer in range } & \frac{(B/H)}{2} + 1 \text{ to } \frac{(B/H)}{3} + 1 \end{aligned} \quad (3)$$

This implies that, for a fixed channel width, as the flow depth is increased, there are fewer regions of upwelling and downwelling and, hence, fewer counter-rotating vortices present in the flow. This will be illustrated and discussed further in the next section.

The free surface in open channel flow presents a kinematic boundary condition through which upwellings or vertical velocity fluctuations cannot penetrate. As a result, when vertical fluctuations approach the free surface, they are redistributed into surface-parallel (streamwise and transverse) velocity fluctuations, hence the strong divergence present over upwelling regions, as previously discussed. The particle tracking velocimetry (PTV) laboratory experiments of Cowen et al. (1995) measured this redistribution of the

vertical velocity fluctuations in an open channel flow. Their Fig. 6 shows the vertical velocity fluctuation decreasing linearly with depth within the top 11 mm beneath the free surface. Their Fig. 5 shows the streamwise fluctuations decaying linearly with depth over the majority of the imaged depth but show an abrupt increase over the top 0.5 mm. In these PTV experiments, the lateral fluctuations were not measured, and therefore no conclusion can be drawn regarding the extent of their enhancement at the free surface.

Figs. 5 and 6 from Cowen et al. (1995) illustrate the essential difficulty in remotely predicting the vertical structure of turbulent intensities. When surface redistribution happens, the turbulence intensity of the streamwise fluctuations on the free surface is elevated above the values of the intensity in the water column, preventing accurate remote prediction of the bulk values. The next section presents the conditions for which the surface redistribution of velocity fluctuations occurs, in addition to a robust method for quantifying the redistribution. Once the extent of the redistribution has been quantified, a method of remotely predicting D_u can be established.

Smooth Bed Experimental Cases

Fig. 2 depicts the normalized streamwise and lateral turbulent intensities plotted against the normalized flow depth measured by the ADV for each smooth bed case. The solid symbols depict u'/u^* , and the hollow symbols depict v'/u^* . In each plot at $z/H = 1$, black (u'/u^*) and gray (v'/u^*) solid symbols depict

the free-surface LSPIV measurements. The solid and dashed lines give Nezu's empirical relations for the streamwise and lateral turbulent intensities, respectively. The friction velocity for each experimental case was estimated via linear extrapolation of the Reynolds stress $\overline{u'w'}$ plot to the bed. This estimate was refined by fitting the total stress, $\tau/\rho = \nu \partial U/\partial z - \overline{(u'w')}$, to a linear distribution, $\tau/\rho = u_*^2(1 - z/H)$, in a least-squares sense.

The departure of these data from Nezu's empirical relations for turbulent intensities is apparent. The best-fit coefficients are $D_u = 1.85$ and $D_v = 1.63$ (Table 1). This difference cannot be attributed to Reynolds number effects because the Reynolds number for Nezu's (1977) experiments ranged from 8,600 to 46,200, and for the present experiments it ranged from 5,000 to 74,000. The variation in exponents is attributed to secondary flows resulting from corner vortices that were present in the wide ($B = 2$ m) channel, which were not present in Nezu's narrower ($B = 0.5$ m) channel (Nezu and Nakagawa 1984, 1993; Nezu and Rodi 1985). From Nezu (1977) and Nezu and Nakagawa (1993), Nezu's best-fit coefficients were fitted from flows that had aspect ratios that ranged from $B/H = 6$ to 23 and flow depths that varied from 0.02 to 0.08 m. This range of aspect ratios is similar to the range in the present experiments ($B/H = 7$ –32); however, the present experiments were conducted with deeper flow depths (0.06–0.31 m). The increased depth relative to Nezu's case means that the corner vortices, which scale with flow depth (Nezu and Rodi 1985), are larger in the present experiments and impact a larger portion of the flow in the spanwise direction, thereby promoting secondary flows. This in turn influences the lateral velocity fluctuations, causing their profiles to deviate from Nezu's relations.

The redistribution of the vertical turbulent velocity fluctuations into surface-parallel components near the free surface is

particularly evident in the fastest, shallowest cases, e.g., $H = 0.6$ –0.15 m, $U_{\text{surf}} = 0.25$, and 0.36 m/s [Figs. 2(h, i, m, n, and o)], for which the streamwise velocity fluctuation increases noticeably near the free surface (where U_{surf} is the centerline mean streamwise surface velocity). The lateral turbulent velocity component for these cases either remains the same or decreases slightly. These results suggest that it is primarily the streamwise component that absorbs most of the vertical momentum. It is hypothesized that the reason the vertical velocity fluctuations are preferentially redistributed to the streamwise component is due to the enhanced velocity and turbulence in the streamwise direction.

Comparing the fastest and shallowest cases [Figs. 2(m–o), $H = 0.06$ –0.15 m, $U_{\text{surf}} = 0.36$ m/s], the magnitude of the free-surface redistribution decreases with increasing flow depth. In the shallowest flow cases, when energetic bursts from the bed reach the free surface, they are strongly coupled with the incipient bursting motion at the bed from which they originated, more so than in deep flows, owing to the shorter water column the burst must travel through on its way to the free surface. Hence, in shallow flows, the bursts are less damped and the surface redistribution is more pronounced. The subsequent effect on the free surface is also more pronounced. Note that the Froude number, which varies from 0.05 to 0.46 for these experimental cases, is not the controlling parameter on the magnitude of the observed free-surface redistribution. Plots (not shown) of the three components of turbulence intensity versus Froude number reveal that the vertical and lateral fluctuations are independent of Froude number for the experimental cases herein, but the streamwise turbulence intensity does increase by approximately 20% over the range. Nezu (2005) gives equations describing the influence of Froude number on the distribution of turbulence between the three component directions as the free

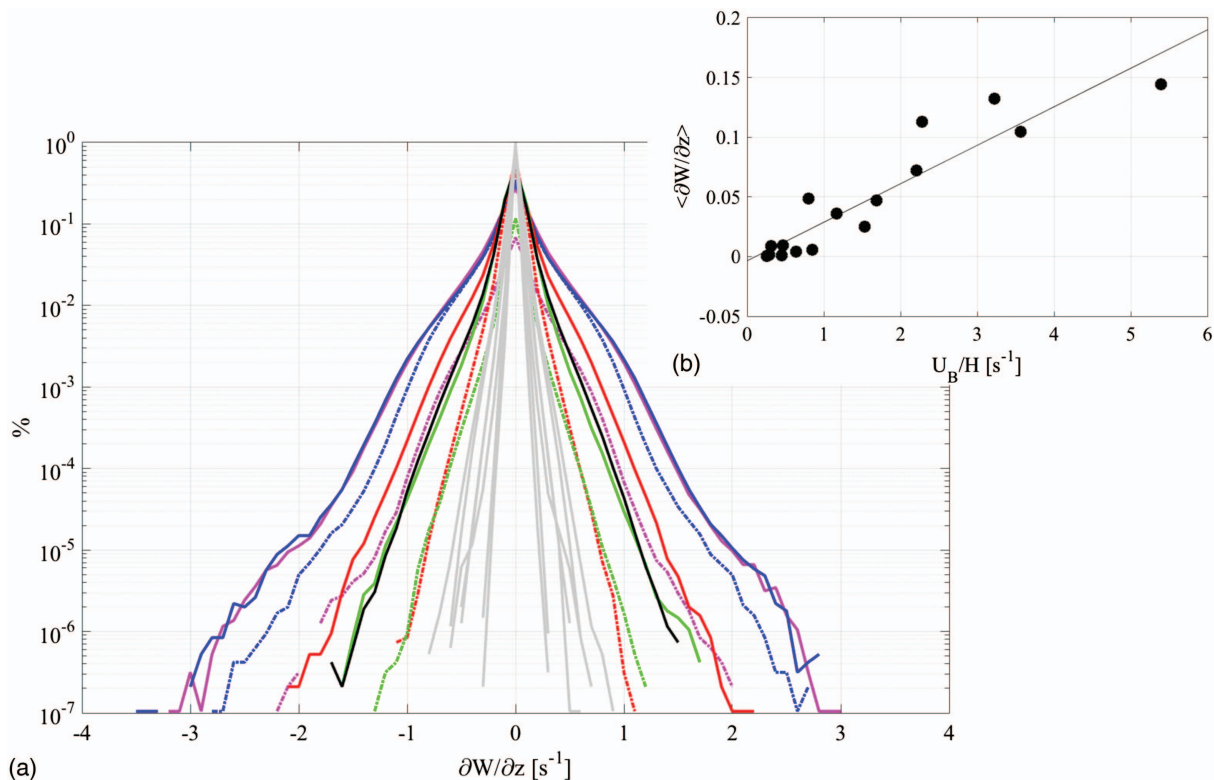


Fig. 3. (Color) (a) Probability density function of free-surface upwelling. Magenta lines, $H = 0.06$ m. Blue lines, $H = 0.10$ m. Red lines, $H = 0.15$ m, Green lines, $H = 0.20$ m. Black lines, $H = 0.30$ m. Gray lines are all experimental cases $U_{\text{surf}} \leq 0.10$ m/s; and (b) depth averaged velocity versus free-surface upwelling.

surface is approached. Variation in the relative distributions is observed for Froude numbers that are much higher than the values obtained here. As will be discussed later, it is the channel width-to-depth aspect ratio, which dictates the number of counter-rotating vortices that are present, that is the dominant parameter describing the redistribution observed in Figs. 2(h, i, m, n, and o).

The assertion that deeper water columns result in reduced levels of surface turbulence is corroborated by Fig. 3, which depicts the probability density function of free-surface divergence. The divergence at the free surface was determined using the continuity relation, $\partial W/\partial z = -(\partial U/\partial x + \partial V/\partial y)$, where U , V , and W indicate the instantaneous streamwise, lateral, and vertical velocity components, respectively. The derivatives on the right-hand side of this expression were calculated from the instantaneous free-surface velocity field measurements obtained from the LSPIV system using a central difference centered on the location where the vertical gradient is calculated. The profiles depicted in Fig. 3 were calculated away from the channel walls ($|y/B| \leq 0.30$) on a subset of images whose temporal length corresponds to several eddy turnover times. Positive values of $\partial W/\partial z$ correspond to upwelling, negative values to downwelling. It is readily apparent that upwelling at the surface is strongest for the shallowest cases ($H = 0.06$ and 0.10 m, magenta and blue lines, respectively) and becomes weaker with increasing flow depth ($H = 0.20$ and 0.30 m, green and black lines, respectively). Again, this can be attributed to bursts traversing a longer water column allowing more time for the turbulence cascade process to redistribute, and dissipate, turbulence structures generated at the bed. Recalling that Shvidchenko and Pender (2001) found that full development of the counter-rotating vortices was achieved in a distance equivalent to approximately 25–50 flow depths, an additional cause for the deeper 0.30 -m cases exhibiting weaker upwelling is that they may not be fully developed. The solid gray lines correspond to experimental cases for which $U_{\text{surf}} \leq 0.10$ m/s. For these cases upwelling and downwelling at the free surface are diminished. This suggests that there is a flow speed below which the bursts are not strong enough to significantly influence the free surface. This result is not surprising because it is generally assumed that the magnitude of secondary flows in an open channel is approximately 3%–5% of the streamwise velocity component (Nezu and Nakagawa 1993; Nezu 2005). The dependence of upwelling on depth-averaged velocity is illustrated in Fig. 3(b).

Fig. 4 depicts an instantaneous snapshot of the free-surface divergence for two flow cases in a contour plot [Fig. 4(a): $H = 0.06$ m and Fig. 4(b): $H = 0.2$ m, both at $U_{\text{surf}} = 0.25$ m/s]. The scale of Fig. 4 has been adjusted to highlight the regions of strongest upwellings and downwellings. Overlaid on the contour plot is the contemporaneous turbulence velocity field. It is evident from the contour plots that the free surface of the shallower flow cases is more densely populated with stronger upwellings and downwellings. These two experimental flow cases have the same flow speed but different depths. Comparison of these two figures shows that the added height in the water column acts to dampen upwellings on the free surface. It is also evident that upwellings and downwellings are organized about the coherent structures present in the flow and that more structures are present in the shallow case than in the deeper case, as suggested by Tamburrino and Gulliver's (1999) relations, given previously.

The coherent structures present in Fig. 4(a) are long, narrow, and well organized. They are the canonical depth-scale counter-rotating vortices, and their shape influences the anisotropy of the free-surface horizontal turbulence components. This can be observed in Fig. 5(a), which depicts the mean free-surface anisotropy for the horizontal turbulence RMS velocities, u'/v' , as measured by

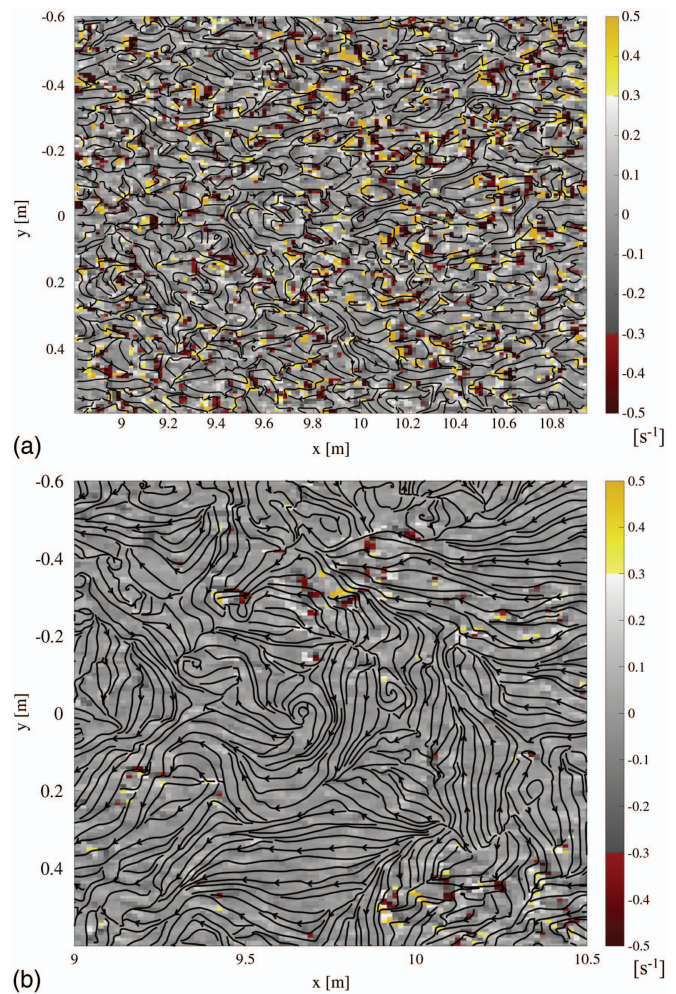


Fig. 4. (Color) Contour plot of free-surface divergence, $\partial W/\partial z$, with simultaneous turbulence velocity field overlaid (u' and v' field): (a) $H = 0.06$ m, $U_{\text{surf}} = 0.25$ m/s; and (b) $H = 0.2$ m, $U_{\text{surf}} = 0.25$ m/s. Yellow corresponds to upwelling, red to downwelling.

the LSPIV system. It is readily observed that the free surface becomes less anisotropic with increasing flow depth. Fig. 5(b) depicts the ratio of the streamwise integral length scale, $L_{1,1,1}$, divided by the transverse integral length scale, $L_{2,2,2}$, where each integral length scale was calculated by integrating the normalized spatial autocorrelation function of the streamwise and transverse turbulent RMS velocities, respectively, given by

$$L_{i,j,k} = \int \frac{\overline{u'_i(x_c - 1/2r_k)u'_j(x_c + 1/2r_k)}}{\sqrt{\overline{u'_i(x_c - 1/2r_k)^2}\overline{u'_j(x_c + 1/2r_k)^2}}} \quad (4)$$

where r = spatial separation vector; x_c = x coordinate about which the correlation is performed; overbar = temporal averaging; and subscripts i, j, k are substituted for a 1 or a 2 to indicate the streamwise or transverse directions, respectively (Variano and Cowen 2008). This quantity is effectively the aspect ratio of the depth scale counter-rotating vortices, and it shows a tendency toward isotropy for increasing depths. Although not shown here, the ratio $L_{1,1,1}/L_{2,2,1}$ showed a similar trend.

In addition to influencing the anisotropy of the free surface, the counter-rotating vortices influence the redistribution of the vertical velocity fluctuations, primarily into the streamwise direction,

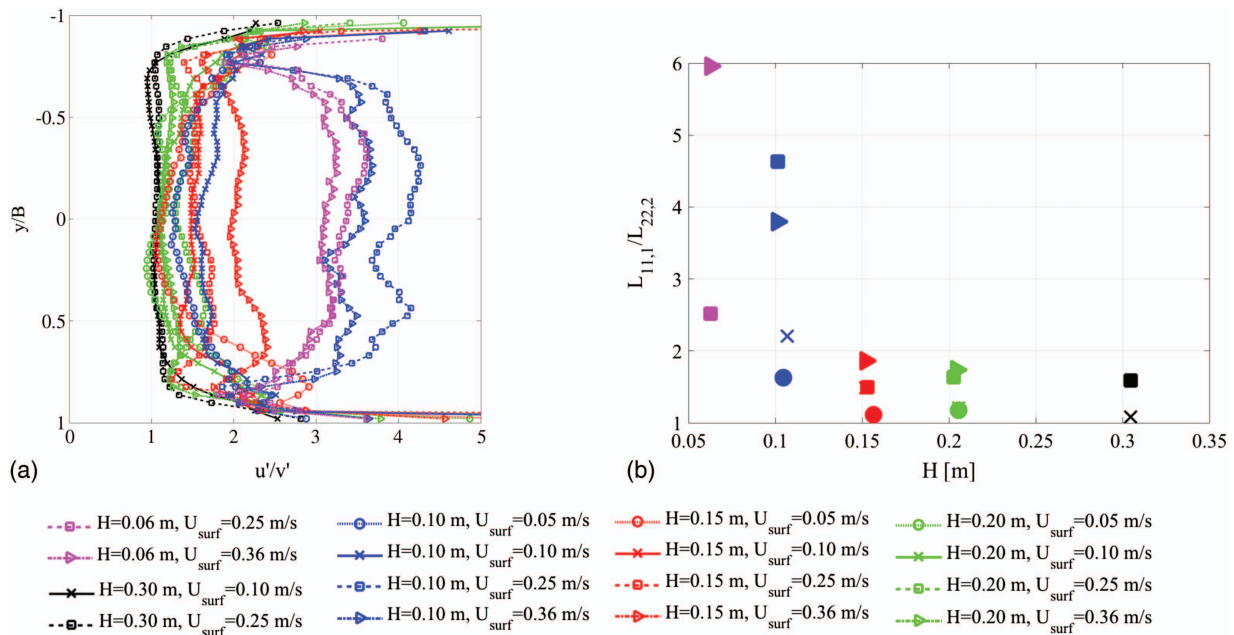


Fig. 5. (Color) (a) Free-surface turbulence anisotropy, u'/v' , for smooth bed cases; and (b) eddy aspect ratio, $L_{11,1}/L_{22,2}$, for smooth bed cases.

as previously discussed. It was observed in Fig. 4 that upwellings and downwellings are organized about the coherent structures present in the flow. Figs. 2(h, i, and m–o) provide evidence that the streamwise velocity fluctuations primarily absorb the redirected vertical velocity fluctuations. The enhanced near-surface streamwise velocity fluctuation is explained through the influence of the counter-rotating vortices bringing strong bed-generated turbulence up to the free surface. Fig. 6 provides a conceptual schematic of the relationships between all the relevant flow parameters.

Remote Sensing Methodology

The free-surface turbulence anisotropy is readily assessed via remote sensing. Because of the interconnected nature of the flow geometry, the counter-rotating structures, and the influence they have on the flow (Fig. 6), the free-surface turbulence anisotropy can be leveraged as a predictor of the redistribution effect. Specifically, the free-surface turbulence anisotropy will be used to predict the increase in the near-surface streamwise velocity fluctuations

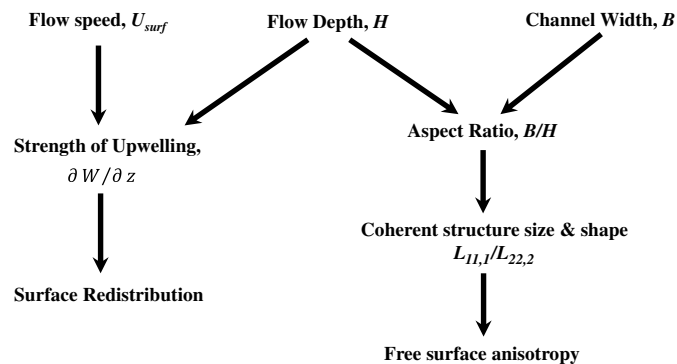


Fig. 6. Schematic describing relationship between relevant flow parameters.

relative to their magnitude in the water column as illustrated in Fig. 7. This is possible because the free-surface turbulence anisotropy can be used to provide information about the geometry of the structures and the flow depth, which in turn is related to the upwelling present on the free surface.

The increase in the streamwise velocity fluctuations relative to their magnitude in the water column is quantified using, $u'_{redistrib} = u'_{freesurface} - u'_{inflectionpoint}$ and is illustrated in Fig. 7. Here, the value of $u'_{inflectionpoint}$ is taken to be the value in the water column just

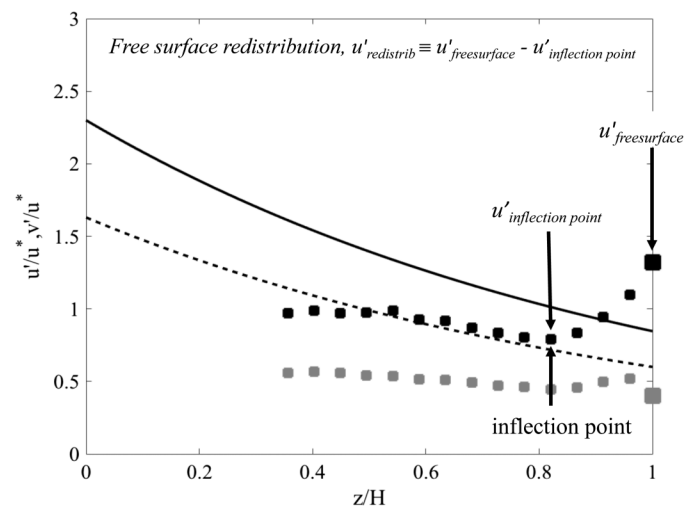


Fig. 7. Illustration of method terminology. The data used in the figure are taken from the $H = 0.06$ m, $U_{surf} = 0.25$ m/s experimental case [seen previously in Fig. 2(h)]. The turbulent intensity for this case is plotted, u'/u^* (black symbols) and v'/u^* (gray symbols). Large black (u'/u^*) and gray (v'/u^*) symbols at $z/H = 1$ are surface LSPIV measurements. Solid black line, $u'/u^* = 2.3 \exp(-z/H)$; dashed black line, $v'/u^* = 1.63 \exp(-z/H)$. (Equation from Nezu 1977.)

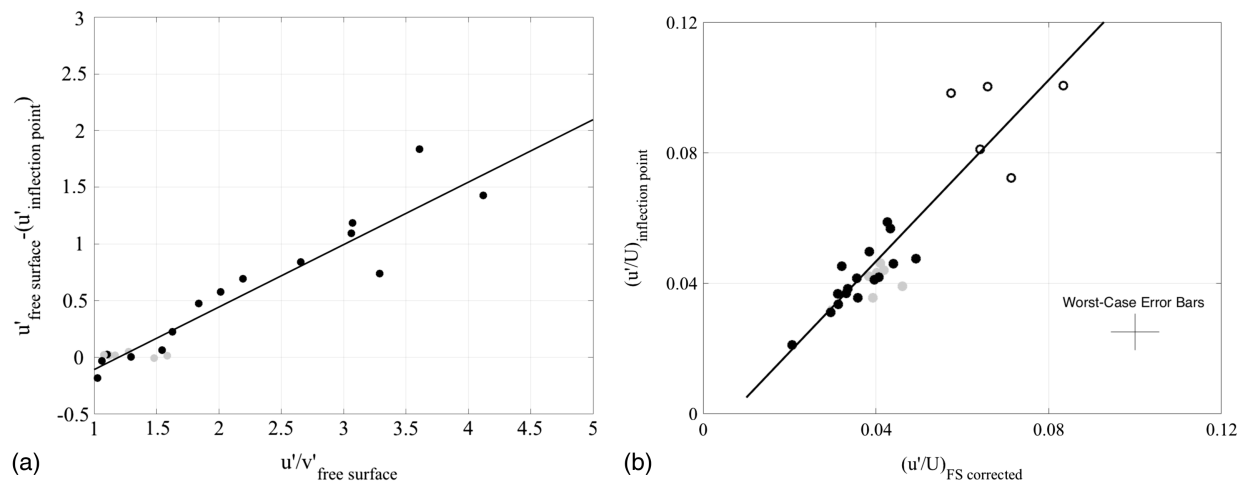


Fig. 8. (a) Free-surface anisotropy versus difference in magnitude between free-surface and near-surface streamwise fluctuation. Solid line: $f(x) = 0.55x - 0.66$, $R^2 = 0.89$; and (b) corrected free-surface turbulence intensity versus near-surface turbulence intensity. Solid line: $f(x) = 1.39x - 0.01$, $R^2 = 0.95$. Black symbols: smooth bed cases ($U_{\text{surf}} > 0.10$ m/s). Gray symbols: smooth bed cases ($U_{\text{surf}} < 0.10$ m/s). Hollow black symbols denote rough bed cases.

before the inflection point in the vertical profile, where the profile starts to increase toward the free surface (arrows in Fig. 7). The difference in magnitudes is plotted against the free-surface anisotropy in Fig. 8(a) and a consistent, strong correlation ($f(x) = 0.55x - 0.66$, $R^2 = 0.89$) is demonstrated for the smooth bed cases (black symbols, $U_{\text{surf}} > 0.10$ m/s, gray symbols, $U_{\text{surf}} < 0.10$ m/s). A number of different flow parameters were explored for a potential fit (e.g., Froude number, aspect ratio, free-surface upwelling); however, it was found that the free-surface anisotropy yielded the best fit.

The correlation given in Fig. 8(a) allows prediction of the increase in the streamwise velocity fluctuations near the free surface. This information can be used to calculate a “corrected” turbulence intensity, given by $(u'_{\text{free surface}} - u'_{\text{redistrib}})/U_{\text{surf}}$. Here, the turbulence intensity is calculated with a mean *surface velocity* rather

than, as defined by Nezu (1977), with the friction velocity. This is because the surface velocity is a quantity that is readily measured remotely. It is common to calculate turbulence intensity with a bulk flow velocity within the turbulence community, and the end result will be given as u'/u^* in accordance with Nezu (1977).

As illustrated in Fig. 8(b), the corrected free-surface turbulence intensity is nearly equivalent to the turbulence intensity measured in the water column at the inflection point, thereby proving the success of using the surface anisotropy to predict the redistribution. The slope of the best-fit line, $f(x) = 1.39x - 0.01$, is close to, but not quite equal to, 1. This is due to the fact that turbulence intensity is being compared at two different elevations in the water column and it naturally increases closer to the bed. This correlation permits conversion of corrected surface values of turbulent intensities to bulk water column values. As illustrated in Fig. 9, the bulk mean turbulence intensity (again this is formed with the maximum near-surface velocity measured by the ADV) is proportional to the previously measured empirical constant, D_u , for each experimental case. Here again the correlation is quite strong, $R^2 = 0.93$.

A method for remotely predicting D_u is therefore established. A summary of the steps is given in what follows:

1. Measure the free-surface turbulence anisotropy, u'/v' , using LSPIV or other appropriate technique. Use the expression given in Fig. 8(a), $u'_{\text{redistrib}} = (u'_{\text{free surface}} - u'_{\text{inflection point}}) = 0.55(u'/v')_{\text{free surface}} - 0.66$, to calculate the increase in the near-surface streamwise velocity fluctuation due to the redistribution effect.
2. Measure U_{surf} and calculate the corrected free-surface turbulence intensity: $(u'/U)_{\text{FS corrected}} = (u'_{\text{free surface}} - u'_{\text{redistrib}})/U_{\text{surf}}$.
3. Use the expression given in Fig. 8(b), $(u'/U)_{\text{inflection point}} = 1.39(u'/U)_{\text{FS corrected}} - 0.01$, to calculate the near-surface turbulence intensity at the inflection point.
4. Use the expression given in Fig. 9, $D_u = 22.94(u'/U)_{\text{inflection point}} + 0.73$, to calculate Nezu's constant, D_u .
5. Predict the vertical variation of the streamwise turbulent intensities using $u'/u^* = D_u \exp(-z/H)$.

A comparison of remotely estimated and measured values of D_u and of the turbulence intensity, u'/u^* , at several elevations above the bed are given in Figs. 10(a and b), respectively. The agreement for both is good.

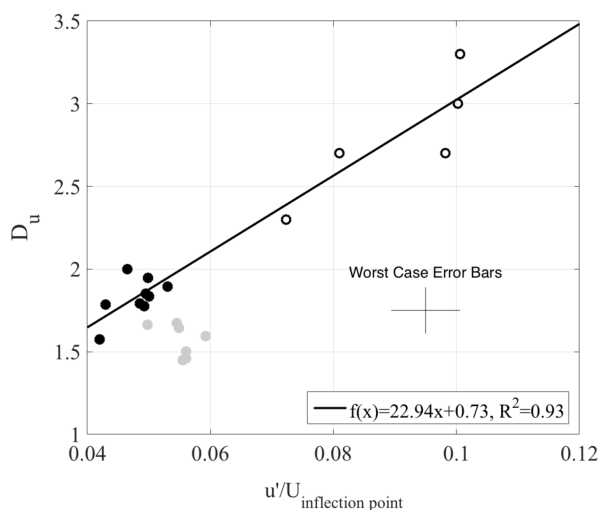


Fig. 9. Near-surface turbulence intensity versus Nezu's constant. Black symbols denote smooth bed cases ($U_{\text{surf}} > 0.10$ m/s). Gray symbols denote smooth bed cases ($U_{\text{surf}} < 0.10$ m/s). Hollow black symbols denote rough bed cases. Solid line: $f(x) = 22.94x + 0.73$, $R^2 = 0.93$.

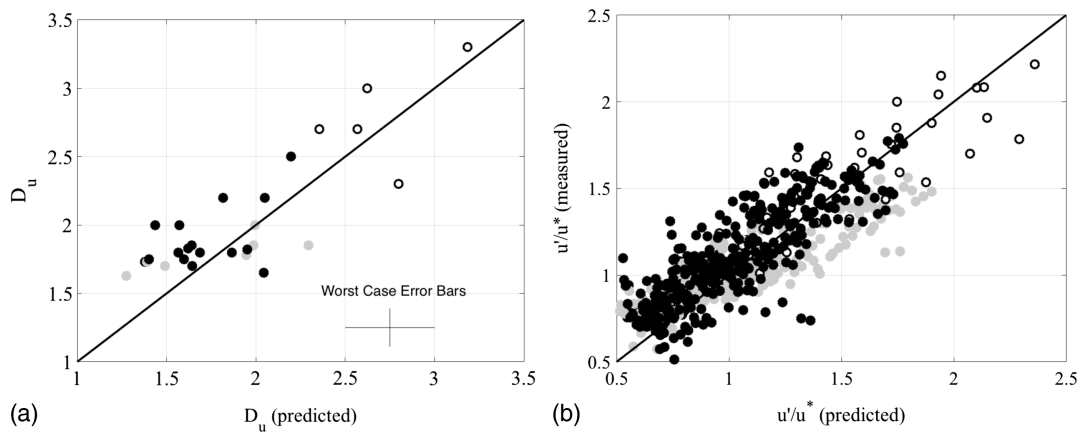


Fig. 10. (a) Predicted versus measured D_u . Solid line: $f(x) = x$; and (b) predicted versus measured u'/u^* . Solid line: $f(x) = x$. Black symbols denote smooth bed cases ($U_{surf} > 0.10$ m/s). Gray symbols denote smooth bed cases ($U_{surf} < 0.10$ m/s). Hollow black symbols denote rough bed cases.

Rough Bed Experimental Cases

The experimental setup of the rough bed cases was such that the gravel bed spanned half of the channel [$y = 0.1-1$ m, see Fig. 1 earlier, and see Fig. 4 in Johnson and Cowen (2016)]. The primary influence that a rough wall or gravel bed can have on a wall-bounded flow, which has been reported extensively in the literature, is to increase the turbulent velocity fluctuations in all three component directions (Balachandar and Bhuiyan 2007; Antonia and Krogstad 2001; Krogstad and Antonia 1999; Krogstad et al. 1992). In particular, the vertical velocity fluctuations are greatly enhanced (e.g., Krogstad et al. 1992). Of particular interest here is how the enhanced vertical velocity fluctuations manifest in terms of upwelling and whether or not the redistribution of these enhanced

vertical velocity fluctuations into surface-parallel components is also enhanced. It has also been demonstrated that the turbulence diffusion terms, which represent the diffusion of turbulence by turbulence in the Reynolds stress transport equations as triple correlation terms, are also enhanced relative to the smooth wall case (Balachandar and Bhuiyan 2007). The net effect is that the turbulence over the rough bed becomes more homogenous (Fig. 12 in Krogstad et al. 1992).

Enhanced velocity fluctuations due to the rough bed are clearly demonstrated in Fig. 11, especially when compared with the results from the smooth bed case (Fig. 2). Note that in each subfigure in Fig. 11, a profile (solid and hollow symbols) measured at $x = 9.9$ m and $y = 0.46$ is shown, in addition to a double-averaged profile (dotted-dashed line) that averages over the spatial variability of

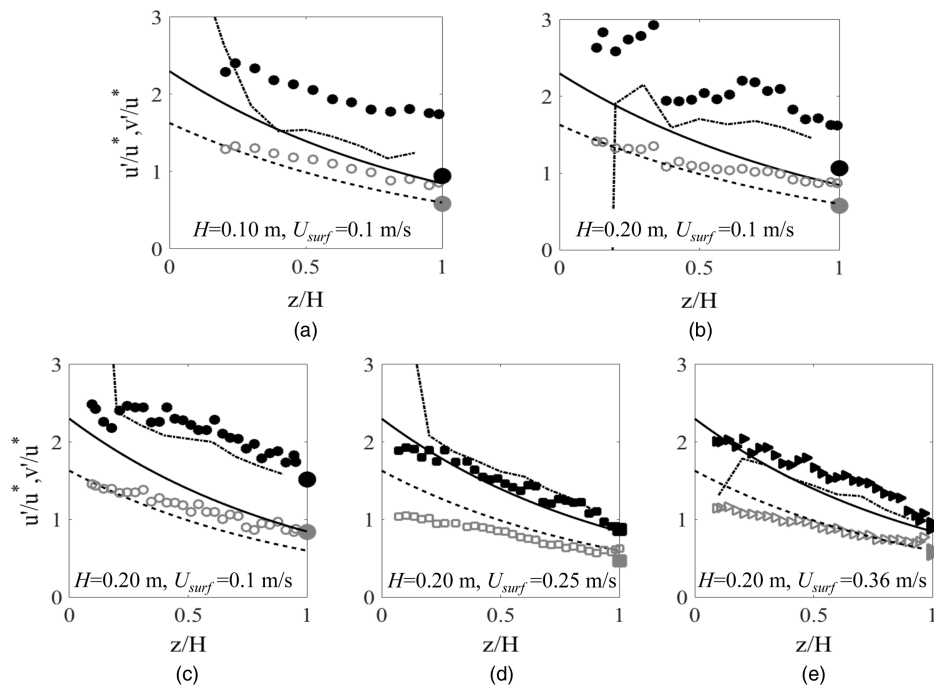


Fig. 11. u'/u^* (solid symbols) and v'/u^* (hollow symbols) local turbulent intensities for rough bed cases. Dotted-dashed colored line is double-averaged streamwise turbulence intensity [see Nikora et al. (2001) for definition]. Large black (u'/u^*) and gray (v'/u^*) filled-in symbols denote surface LSPIV measurements. Solid black line, $u'/u^* = 2.3 \exp(-z/H)$; dashed black line, $v'/u^* = 1.63 \exp(-z/H)$. (Equation from Nezu 1977.)

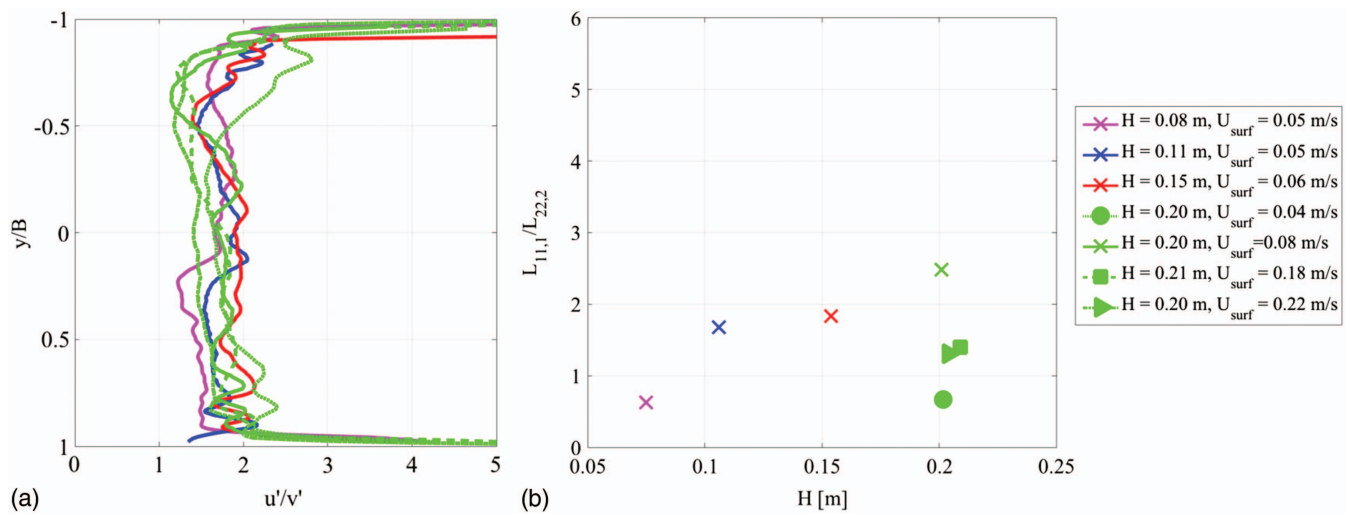


Fig. 12. (Color) (a) Free-surface turbulence anisotropy, u'/v' , for rough bed cases; and (b) eddy aspect ratio, $L_{1,1,1}/L_{2,2,2}$, for rough bed cases.

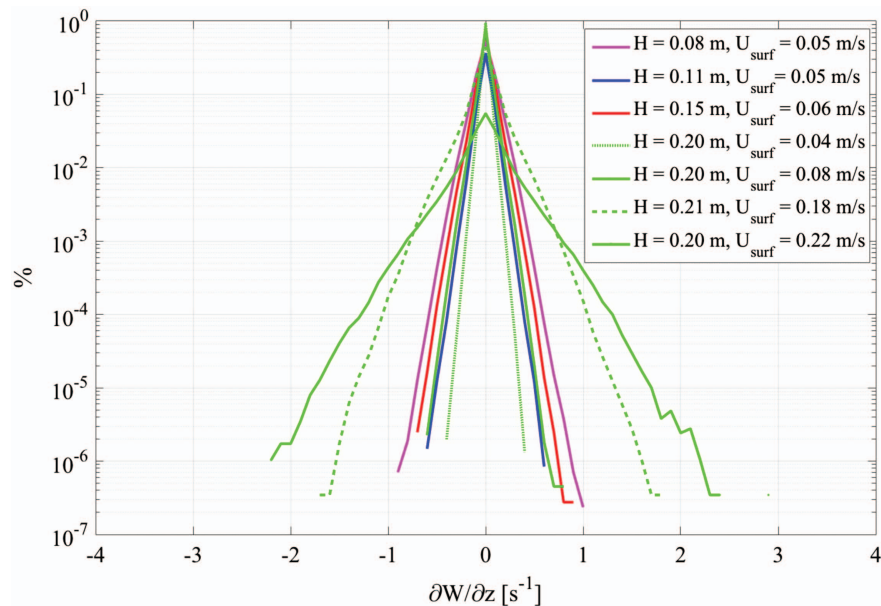


Fig. 13. (Color) Probability density function of free-surface upwelling for rough bed cases. Magenta lines, $H = 0.08$ m. Blue lines, $H = 0.11$ m. Red lines, $H = 0.15$ m. Green lines, $H = 0.20$ m.

the gravel bed (Nikora et al. 2001). The tendency toward isotropy on the free surface can also be observed in Figs. 12(a and b). The free-surface anisotropy for the rough bed cases is roughly $u'/v' \approx 1.7$. Upwelling at the free surface over the rough bed (Fig. 13) is approximately the same magnitude or greater as compared to the smooth bed cases (Fig. 3). Yet, despite the enhanced velocity fluctuations and similar magnitude of upwelling on the free surface, it appears that the enhancement of surface fluctuations, which was previously attributed to organized coherent structures, is not here. Examination of Figs. 11(a–e) shows that neither the streamwise nor the lateral velocity fluctuations increase toward the free surface. This seeming contradiction is attributed to the absence of a counter-rotating structure in these flows. The higher degree of free-surface isotropy indicates their absence, and it is presumed that they have been stirred out by the stronger roughness-generated turbulence levels.

However, despite the absence of counter-rotating flow structures in the rough bed cases, the methodology developed earlier is still applicable to these experiments. Because there is no free-surface fluctuation enhancement by counter-rotating vortices, the first step of the methodology is skipped and the remaining steps are performed starting with the free-surface value of the turbulence intensity, $(u'_{\text{freesurface}})/U_{\text{surf}}$, measured directly. The hollow black circles in Figs. 8(b), 9, and 10(a and b) depict the accordance of the rough bed experimental values with the rest of the developed methodology. Again, the agreement between the remotely estimated and measured values of D_u and the turbulence intensity is good.

Discussion

The methodology described earlier, namely, the use of free-surface anisotropy to confirm the existence of streamwise counter-rotating

vortices in open channel flows and to describe the free-surface upwelling and redistribution they cause, is a novel and intriguing idea that warrants further study in the field. It permits remote estimation of the vertical variation of streamwise turbulence intensity, which can be used in conjunction with the method of Johnson and Cowen (2017) to predict the friction velocity and bed shear stress entirely from remote sensing techniques. This capability is fundamental in remote studies of sediment transport.

In considering field applications of this remote sensing methodology, caution should be exercised for very slow-moving flows. Fig. 3 suggests that upwelling at the free surface will be small. Figs. 8–10 (gray circles) further suggest that there may be some low Reynolds number effects in applying this methodology. In addition, it should be kept in mind that because this technique is empirical and based on specific flume experiments at low Froude numbers, further measurements may be required to confirm the proposed equations in specific field environments.

There are two broader implications of this work. The first is that the turbulence on the free surface can yield clues as to the bottom composition. As seen in Figs. 5(a and b), if the turbulence on the free surface is highly anisotropic, this may be an indicator of streamwise counter-rotating vortices over a smooth or sandy bottom. If the spatial locations of bands of upwelling and downwelling are relatively stable on the free surface [unlike what was observed in Figs. 4(a and b)], this may indicate a bed with stable bedforms. If they meander spatially, this may indicate planar bed conditions. If the turbulence on the free surface is more isotropic, this may be an indicator of a gravel or otherwise roughened bottom. A stable train of isotropic eddies (as in a Kármán vortex street) that is surrounded by longer anisotropic eddies may indicate a bottom protuberance, as seen in Fig. 3 of Brocchini and Peregrine (2001). Exploiting the anisotropy of the free-surface signature in this manner may lead to a quick method of assessing bathymetric surface composition and local bathymetry change.

The second implication of this work is subtle. It has long been assumed that the long streamwise counter-rotating structures [seen in Fig. 9 of Shvidchenko and Pender (2001) and Fig. 5.19 of Nezu and Nakagawa (1993)] are steady, well-organized structures that meander spatially as they move downstream. However, the upwelling contour plots of Fig. 4 suggest that the bands of upwelling and downwelling seen are not steady but are intermixed spatially in a seemingly random, chaotic manner. Indeed, the instantaneous turbulent velocity fields support this finding. Additional surface velocity field measurement results in rivers are needed to clarify this assertion. However, this picture is more consistent with the pattern of sweeps and ejections that have been heavily studied in boundary layer flows and are believed to give rise to the counter-rotating structures.

Conclusion

With the aim of developing a remote methodology for predicting the vertical variation of streamwise turbulence intensity in open channel flows, several laboratory experiments were conducted for a range of aspect ratios ($B/H = 6.6\text{--}31.9$), Reynolds numbers ($R_H = 5,000\text{--}70,000$), and bed roughness conditions. It was demonstrated that as the vertical velocity fluctuations approach the free surface, they are redistributed primarily into the streamwise direction, causing an increase in the vertical profiles of turbulence intensity near the free surface. This redistribution effect increases with decreasing flow depth, as does the strength of the free-surface upwelling. These experiments also showed that for smooth bed open channel flows, the streamwise counter-rotating

structures cause anisotropy in the free surface turbulence, which becomes pronounced with decreasing flow depth. A methodology was developed to quantify this redistribution by leveraging the free-surface anisotropy, and, once corrected for, it was found that the free-surface turbulence intensity is proportional to the empirical constant used in Nezu's relation. Thus, a method of remotely predicting the vertical structure of the streamwise turbulence intensity is enabled.

Data Availability Statement

Some or all data, models, or code generated or used during the study are available from the corresponding author by request.

Acknowledgments

This work was supported by the National Institutes for Water Resources (Grant No. 2012NY189G). Johnson gratefully acknowledges the support of the NRC Associateship, National Sloan Foundation, the DeFrees Fellowship, and the Colman Fellowship. The authors would like to acknowledge the hard work of Tim Brock, Paul Charles, and Jack Powers in facilitating the experiments.

Notation

The following symbols are used in this paper:

- A = channel cross-sectional area;
- B = channel width;
- D_u, D_v, D_w = Nezu (1977) empirical coefficients appearing in turbulence intensity equation;
- D_{50} = median gravel bed element diameter;
- E = Nezu (1977) empirical constant appearing in dissipation equation;
- H = flow depth;
- i, j, k = coordinate direction indices;
- $L_{1,1,1}$ = streamwise integral length scale;
- $L_{2,2,2}$ = spanwise integral length scale;
- $L_{2,2,1}$ = spanwise integral length scale calculated in the streamwise direction;
- Q = volumetric discharge;
- $R = (U_m H)/\nu$ = Reynolds number formed with flow depth and bulk mean velocity;
- $R_H = (U_B H)/\nu$ = Reynolds number formed with flow depth and depth-averaged velocity;
- r = spatial separation vector in integral length scale calculation;
- U = instantaneous streamwise velocity;
- $U_B = \int_0^H \langle U(z) \rangle / H dz$ = depth-averaged velocity;
- $U_m = Q/A = \int_0^B U_B / A dy$ = bulk mean velocity;
- U_{surf} = mean centerline surface streamwise velocity;
- u^* = friction velocity;
- u = streamwise velocity fluctuation;
- u' = streamwise root-mean square velocity;
- V = instantaneous lateral velocity;
- v = lateral velocity fluctuation;
- v' = lateral root mean square velocity;
- W = instantaneous vertical velocity;
- w = vertical velocity fluctuation;

w' = vertical root mean square velocity;
 x = streamwise direction;
 y = lateral direction;
 z = vertical direction;
 Δt = elapsed time between image pairs; and
 ε = mean dissipation of turbulent kinetic energy.

References

- Antonia, R. A., and P. Å. Krogstad. 2001. "Turbulence structure in boundary layers over different types of surface roughness." *Fluid Dyn. Res.* 28 (2): 139–157. [https://doi.org/10.1016/S0169-5983\(00\)00025-3](https://doi.org/10.1016/S0169-5983(00)00025-3).
- Balachandar, R., and F. Bhuiyan. 2007. "Higher-order moments of velocity fluctuations in an open-channel flow with large bottom roughness." *J. Hydraul. Eng.* 133 (1): 77–87. [https://doi.org/10.1061/\(ASCE\)0733-9429\(2007\)133:1\(77\)](https://doi.org/10.1061/(ASCE)0733-9429(2007)133:1(77)).
- Brocchini, M., and D. H. Peregrine. 2001. "The dynamics of strong turbulence at free surfaces. 1: Description." *J. Fluid Mech.* 449 (Dec): 225–254.
- Cardoso, A. H., W. H. Graf, and G. Gust. 1989. "Uniform flow in a smooth open channel." *J. Hydraul. Res.* 27 (5): 603–616. <https://doi.org/10.1080/00221688909499113>.
- Carling, P. A., Z. Cao, M. J. Holland, D. A. Ervine, and K. Babaeyan-Koopaei. 2002. "Turbulent flow across a natural compound channel." *Water Resour. Res.* 38 (12): 6–1–6–11. <https://doi.org/10.1029/2001WR000902>.
- Carvalho, E., R. Maia, and M. F. Proença. 2010. "Shear stress measurements over smooth and rough channel beds." In Vol. 2010 of *Proc., River Flow 2010*, 367–375. Beijing: IAHR.
- Cowen, E. A., and S. G. Monismith. 1997. "A hybrid digital particle tracking velocimetry technique." *Exp. Fluids* 22 (3): 199–211. <https://doi.org/10.1007/s003480050038>.
- Cowen, E. A., S. G. Monismith, and J. R. Koseff. 1995. "Digital particle tracking velocimetry measurements very near a free-surface." In *Air water gas transfer*, 135–144. Hanau, Germany: Aeon Verlag and Studio.
- Dittrich, A., and K. Koll. 1997. "Velocity field and resistance of flow over rough surfaces with large and small relative submergence." *Int. J. Sediment Res.* 12 (3): 21–33.
- Efron, B., and R. J. Tibshirani. 1994. Vol. 57 of *An introduction to the bootstrap*, Boca Raton, FL: CRC Press.
- Johnson, E. 2015. "The remote monitoring of surface velocity, bathymetry and discharge in rivers and open channel flows." Ph.D. dissertation, School of Civil and Environmental Engineering, Cornell Univ.
- Johnson, E. D., and E. A. Cowen. 2016. "Remote monitoring of volumetric discharge employing bathymetry determined from surface turbulence metrics." *Water Resour. Res.* 52 (3): 2178–2193. <https://doi.org/10.1002/2015WR017736>.
- Johnson, E. D., and E. A. Cowen. 2017. "Estimating bed shear stress from remotely measured surface turbulent dissipation fields in open channel flows." *Water Resour. Res.* 53 (3): 1982–1996. <https://doi.org/10.1002/2016WR018898>.
- Knight, D. W., and K. Shiono. 1990. "Turbulence measurements in a shear layer region of a compound channel." *J. Hydraul. Res.* 28 (2): 175–196. <https://doi.org/10.1080/00221689009499085>.
- Krogstad, P. Å., R. A. Antonia, and L. W. B. Browne. 1992. "Comparison between rough-and smooth-wall turbulent boundary layers." *J. Fluid Mech.* 245 (–1): 599–617. <https://doi.org/10.1017/S0022112092000594>.
- Krogstad, P. Å., and R. A. Antonia. 1999. "Surface roughness effects in turbulent boundary layers." *Exp. Fluids* 27 (5): 450–460. <https://doi.org/10.1007/s003480050370>.
- Nezu, I. 1977. "Turbulent structure in open-channel flows." Ph.D. dissertation, Dept. of Civil Engineering, Kyoto Univ.
- Nezu, I. 2005. "Open-channel flow turbulence and its research prospect in the 21st century." *J. Hydraul. Eng.* 131 (4): 229–246. [https://doi.org/10.1061/\(ASCE\)0733-9429\(2005\)131:4\(229\)](https://doi.org/10.1061/(ASCE)0733-9429(2005)131:4(229)).
- Nezu, I., and H. Nakagawa. 1984. "Cellular secondary currents in straight conduit." *J. Hydraul. Eng.* 110 (2): 173–193. [https://doi.org/10.1061/\(ASCE\)0733-9429\(1984\)110:2\(173\)](https://doi.org/10.1061/(ASCE)0733-9429(1984)110:2(173)).
- Nezu, I., and H. Nakagawa. 1993. *Turbulence in open channel flows*. Rotterdam, Netherlands: A.A. Balkema.
- Nezu, I., and W. Rodi. 1985. "Experimental study on secondary currents in open channel flows." In Vol. 2 of *Proc., 21st IAHR Congress*, 115–119. Beijing: IAHR.
- Nezu, I., and W. Rodi. 1986. "Open-channel flow measurements with a laser Doppler anemometer." *J. Hydraul. Eng.* 112 (5): 335–355. [https://doi.org/10.1061/\(ASCE\)0733-9429\(1986\)112:5\(335\)](https://doi.org/10.1061/(ASCE)0733-9429(1986)112:5(335)).
- Nikora, V., D. Goring, I. McEwan, and G. Griffiths. 2001. "Spatially averaged open-channel flow over rough bed." *J. Hydraul. Eng.* 127 (2): 123–133. [https://doi.org/10.1061/\(ASCE\)0733-9429\(2001\)127:2\(123\)](https://doi.org/10.1061/(ASCE)0733-9429(2001)127:2(123)).
- Nikora, V. I., and G. M. Smart. 1997. "Turbulence characteristics of New Zealand gravel-bed rivers." *J. Hydraul. Eng.* 123 (9): 764–773. [https://doi.org/10.1061/\(ASCE\)0733-9429\(1997\)123:9\(764\)](https://doi.org/10.1061/(ASCE)0733-9429(1997)123:9(764)).
- Rodríguez, J. F., and M. H. García. 2008. "Laboratory measurements of 3-D flow patterns and turbulence in straight open channel with rough bed." *J. Hydraul. Res.* 46 (4): 454–465. <https://doi.org/10.3826/jhr.2008.2994>.
- Roy, A. G., T. Buffin-Belanger, H. Lamarre, and A. D. Kirkbride. 2004. "Size, shape and dynamics of large-scale turbulent flow structures in a gravel-bed river." *J. Fluid Mech.* 500 (Apr): 1–27. <https://doi.org/10.1017/S0022112003006396>.
- Shvidchenko, A., and G. Pender. 2001. "Macroturbulent structure of open-channel flow over gravel beds." *Water Resour. Res.* 37 (3): 709–719. <https://doi.org/10.1029/2000WR900280>.
- Soulsby, R. L. 1981. "Measurements of the Reynolds stress components close to a marine sand bank." *Mar. Geol.* 42 (1–4): 35–47. [https://doi.org/10.1016/0025-3227\(81\)90157-2](https://doi.org/10.1016/0025-3227(81)90157-2).
- Sukhodolov, A., M. Thiele, and H. Bungartz. 1998. "Turbulence structure in a river reach with sand bed." *Water Resour. Res.* 34 (5): 1317–1334. <https://doi.org/10.1029/98WR00269>.
- Sukhodolov, A. N., J. J. Fedele, and B. L. Rhoads. 2006. "Structure of flow over alluvial bedforms: An experiment on linking field and laboratory methods." *Earth Surf. Processes Landforms* 31 (10): 1292–1310. <https://doi.org/10.1002/esp.1330>.
- Tamburrino, A., and J. S. Gulliver. 1999. "Large flow structures in a turbulent open channel flow." *J. Hydraul. Res.* 37 (3): 363–380. <https://doi.org/10.1080/00221686.1999.9628253>.
- Tominaga, A., I. Nezu, K. Ezaki, and H. Nakagawa. 1989. "Three-dimensional turbulent structure in straight open channel flows." *J. Hydraul. Res.* 27 (1): 149–173. <https://doi.org/10.1080/00221688909499249>.
- Tominaga, A., and T. Sakaki. 2010. "Evaluation of bed shear stress from velocity measurements in gravel-bed river with local non-uniformity." In *Proc., River Flow 2010*, edited by A. Dittrich, K. Koll, J. Aberle, and P. Geisenhainer, 187–194. Rotterdam, Netherlands: A. A. Balkema.
- Variano, E. A., and E. A. Cowen. 2008. "A random-jet-stirred turbulence tank." *J. Fluid Mech.* 604 (Jun): 1–32. <https://doi.org/10.1017/S0022112008000645>.